journal

J. Am. Ceram. Soc., 95 [1] 392–402 (2012)
DOI: 10.1111/j.1551-2916.2011.04802.x

Characterizing Three-Dimensional Textile Ceramic Composites Using Synchrotron X-Ray Micro-Computed-Tomography

Hrishikesh Bale,[‡,§] Matthew Blacklock,[¶] Matthew R. Begley,[¶] David B. Marshall,[||] Brian N. Cox,[||] and Robert O. Ritchie[‡,§,†]

[‡]Department of Materials Science and Engineering, University of California, Berkeley, CA 94720

[§]Materials Sciences Division, Lawrence Berkeley National Laboratory, Berkeley, CA 94720

[¶]Department of Mechanical Engineering, University of California, Santa Barbara, CA 93106

[||]Teledyne Scientific Company, Thousand Oaks, CA 91360

Three-dimensional (3-D) images of two ceramic-matrix textile composites were captured by X-ray micron-resolution computed tomography (μCT) on a synchrotron beamline. Compared to optical images of sections, CT data reveal comprehensive geometrical information about the fiber tows; information at smaller scales, on matrix voids, individual fibers, and fiber coatings, can also be extracted but image artifacts can compromise interpretation. A statistical analysis of the shape and positioning of the fiber tows in the 3-D woven architecture is performed, based on a decomposition of the spatial variations of any geometrical characteristic of the tows into non-stochastic periodic trends and non-periodic stochastic deviations. The periodic trends are compiled by exploiting the nominal translational invariance of the textile, a process that maximizes the information content of the relatively small specimens that can be imaged at high resolution. The stochastic deviations (or geometrical defects in the textile) are summarized in terms of the standard deviation of any characteristic at a single point along the axis of a tow and correlations between the values of deviations at two different points on the same or different tows. The tow characteristics analyzed consist of the coordinates of the centroids of a tow, together with the area, aspect ratio, and orientation of its cross-section. The tabulated statistics are sufficient to calibrate a probabilistic generator (detailed elsewhere) that can create virtual specimens of any size that are individually distinct but share the statistical characteristics of the small specimens analyzed by X-ray μCT. The data analysis presented herein forms the first step in formulating a virtual test of textile composites, by providing the statistical information required for realistic description of the textile reinforcement.

I. Introduction

TEXTILE composites with fiber tows woven or braided into two-dimensional (2-D) and three-dimensional (3-D) architectures are increasingly important material options for many types of structures. For high performance and reliability, a key issue is irregularities or geometrical defects in the textile reinforcement, which trigger failure mechanisms and compromise strength and life (e.g., [1–8]). The defects can be substantial perturbations of the ideal architecture. A critical step toward being able to control geometrical defects and predict their influence on performance is measuring and characterizing their type and statistical distribution, a task that has proven extremely difficult using conventional imaging techniques applied to serial sections. Critical internal defects include small volumes of local misalignment of the fiber tows with respect to the nominal load axis (or axis of the fabric) and variations in tow position and tow cross-section. In this article, we address full statistical characterization of geometrical defects at the scale of individual tows in a representative 3-D woven composite, exploiting micron-resolution computed micro-tomography (μCT) images captured on a hard X-ray synchrotron beamline.

The composites studied represent a new class of integrally woven ceramic matrix composites for high-temperature applications,[9] where both strength and thermal conductivity are important; all defects that affect either must ultimately be measured, including geometrical defects, porosity and microcracking (inter-laminar, within tows, and at interfaces).[10–14] Spatial scales span at least the range 1 μm–1 mm. Prior studies have applied μCT to measure certain characteristics of textile geometry and tow deformation,[15–17] as well as porosity[18] and its changes during processing steps.[18,19] These and other studies have also addressed achieving feature definition in ceramic composites,[20] which is often made difficult by low X-ray absorption contrast between the constituent materials. In this work, fiber tows are made to stand out by imaging composites with partially formed matrices.

The data used in this article, acquired using μCT, yield 3-D images of specimens that are 1–10 mm in linear dimension with a spatial resolution of ~2 μm in the available beamline. Resolution down to 0.5 μm has been reported elsewhere.[10,21] Structural applications of textile composites generally involve component dimensions of 0.1–10 m, which are $10–10^4$ times larger than the dimensions (1–10 mm) of the repeating unit of the textile architecture (unit cell). The highest resolution 3-D imaging methods, including the tomography method used herein or methods based on serial sectioning (e.g., [22,23]), can only deal with specimens similar in size to, or smaller than, a single unit cell.

A key challenge is therefore to develop probabilistic methods of predicting the stochastic variations of material microstructure over component-scale volumes, using data that are acquired for small specimens. The statistical analysis of this article is the first step toward such a probabilistic model. For descriptions of tow architecture, the periodicity that is present

R. Kerans—contributing editor

Manuscript No. 29420. Received March 07, 2011; approved July 21, 2011.

This work was supported by the Air Force Office of Scientific Research (Dr. Ali Sayir) and NASA (Dr. Anthony Calomino) under the National Hypersonics Science Center for Materials and Structures (AFOSR Contract No. FA9550-09-1-0477). We acknowledge the use of the X-ray synchrotron micro-tomography beam line (8.3.2) at the Advanced Light Source (ALS) at the Lawrence Berkeley National Laboratory, which is supported by the Office of Science of the U.S. Department of Energy under contract No. DE AC02 05CH11231.

[†]Author to whom correspondence should be addressed. e-mail: roritchie@lbl.gov

in statistically averaged quantities can be exploited to maximize the information content of images. Tow statistics analyzed consist of the loci of the centroid or axis of each tow and the area, aspect ratio, and orientation of its cross-section. The correlations of deviations along a tow and between tows are computed. A geometry generator (or reconstruction algorithm) that uses the data to create stochastic replicas of the tow structure (virtual specimens) that are much larger than the unit cell will be published elsewhere.

An ancillary study of the general potential of X-ray μCT addresses the question of what contrast and resolution can be achieved in imaging the constituents of typical SiC-fiber and carbon-fiber composites with BN fiber coatings and/or SiC matrices. Image quality limits the types of irregularity that can be measured in the fiber reinforcement and the degree to which the spatial distribution of matrix material and matrix porosity can be measured.

II. Experimental Methods

(1) Materials and Sample Preparation

Two textile-based ceramic composites were selected for study, both with 3-D woven architecture. The first composite was reinforced with multifilament SiC fiber tows (Hi-Nicalon Type-S) in a woven layer-to-layer interlock structure. This composite was processed in several stages. First, a coating of BN ~0.5 μm thick, to serve as a debond layer for toughening, was deposited on the fibers in the woven preform by chemical vapor infiltration (CVI). Then the preform was infiltrated with SiC by CVI, depositing some material on individual fibers in the interior regions of each tow before sealing the tow perimeter and building up a layer about 10 μm thick encasing each tow. This layer was sufficient to form a continuous "matrix" that bonded the fiber tows together where they touched one another, while leaving relatively large gaps between fiber tows in other regions. These gaps were then infiltrated with SiC using multiple cycles of infiltration and heat treatment of a slurry of SiC particles in a polymer precursor for SiC (alylhydridopolycarbosilane, AHPCS). In this process, the shrinkage of the polymer precursor during heat treatment (pyrolysis) creates cracks, which allow access for infiltrating additional polymer slurry in subsequent cycles. With increasing cycles, a matrix with near full density can be approached asymptotically, typically after ~10 cycles. The efficiency of this process and the quality of the final matrix depend on the distribution of shrinkage cracks left after each cycle. To assess the potential for using synchrotron-based micro-tomography to follow the progression of densification and map the distributions of material and void space during these polymer infiltration cycles, two samples with dimensions ~3 × 4 × 5 mm were cut with a diamond saw from the composite at different stages of processing, one after the CVI SiC process step and the other after the first polymer infiltration/heat-treatment cycle. The cut surfaces were diamond polished to a mirror finish.

The second composite, used for characterization of fiber tow architecture, was reinforced with carbon fibers (T300-6K tows with filaments of diameter ~7 μm) in a three-layer angle interlock woven structure (fully defined below) of thickness ~1.2 mm. The carbon fiber preform was infiltrated first with pyrolytic carbon as a debond layer on the individual fibers and then with CVI SiC, which sealed the fiber tows and formed an initial layer of matrix ~40 μm thick that rigidized the preform. In this material, the remaining gaps between the fiber tows were not filled with matrix. This partially processed system gives high contrast and clear definition of fiber tow perimeters in the synchrotron images, which enables the use of semi-automated methods of image analysis. Even though the matrix was not fully formed, the preform is already rigidified by the initial SiC layer. If matrix formation were completed, the geometry of the preform would not change from this rigidified structure. Two rectangular samples, one of dimensions 8 × 25 mm with longer side parallel to the warp fiber direction, and the other of dimensions 5 × 25 mm with the longer side parallel to the weft direction, were cut from a large plate of the composite. Both were mounted with the longer dimension parallel to the axis of rotation of the tomography stage. The sample with the warp tows parallel to the axis of rotation and the weft tows in the transverse direction was used for the statistical analysis of tow geometry. In the region imaged, there were five warp tows and 12 weft tows.

(2) Image Acquisition by Synchrotron X-Ray Micro-Computed-Tomography

The X-ray μCT was conducted on the hard X-ray tomography beamline (number 8.3.2) at the Advanced Light Source (Lawrence Berkeley National Laboratory, Berkeley, CA). The beamline receives tunable X-rays in the energy range 8–40 keV from a superconducting bend magnet. Movable monochromator optics provide either monochromatic or polychromatic X-rays. The images reported herein were collected using monochromatic X-rays of energy 21 keV, for which the X-ray transmission through the subject textile-based ceramic composites over the largest path length used (8 mm) was ~20%. The X-ray transmission images were acquired using a $CdWO_4$ scintillator to convert transmitted X-rays to visible light, which was then reflected into an optical microscope [Fig. 1(b)]. Images were recorded in 14 bit format with 4.4 μm pixel resolution.

The stage is equipped with a vertical translation system which allows for tiled scanning. For the three-layer angle-interlock composite, five tiled scans were collected, covering a sample height of 13 mm. For each scan, the sample was rotated by 180° in steps of 0.125°, giving 1440 exposures over a period of about 60–90 min. The transmission images thus captured were used for reconstructing two-dimensional slices normal to the rotation axis using a commercial reconstruction code (Octopus v8; IIC UGent, Zwijnaarde, Belgium). The reconstruction takes ~2.2 s per slice on an eight processor Pentium Xeon 64-bit personal computer (Intel Corporation, Santa Clara, CA).

The entire sample data set contained 3111 axial slices (415 × 1905 pixels) at a 4.4 μm/pixel resolution, amounting to 24 GB of data. Since further data analysis involved 3-D computations that led to memory demands that exceed the available resources, the original dataset was rescaled to an isotropic voxel size of 8.8 μm. The rescaling was performed through a 2 × 2 × 2 3-D Lanczos filter (a low pass multivariate interpolation filter).[24]

Some of the 2-D slices contain reconstruction artifacts which were reduced by processing the data using a 3-D median filter.[††] By applying contrast enhancement filters and edge-preserving smoothing algorithms, the regions in the tomographic slices with lower contrast were enhanced. The processed 2-D slice data serve as input for the methods described below for extracting information about tow geometry.

III. The Information Content of Images

(1) SiC–SiC Composite

Data from the SiC–SiC composite were used to reconstruct and render a 3-D region, illustrating the potential for monitoring the distribution of infiltrated matrix material and remaining porosity over relatively large volumes during processing. 3-D images of the composite structure after the CVI SiC processing step and after the first polymer infiltration/heat-treatment cycle are shown in Figs. 2(a) and (b). Recon-

[††]3-D median filter eliminates speckle and noise by replacing each pixel value in 3-D space with the median of its neighboring pixels

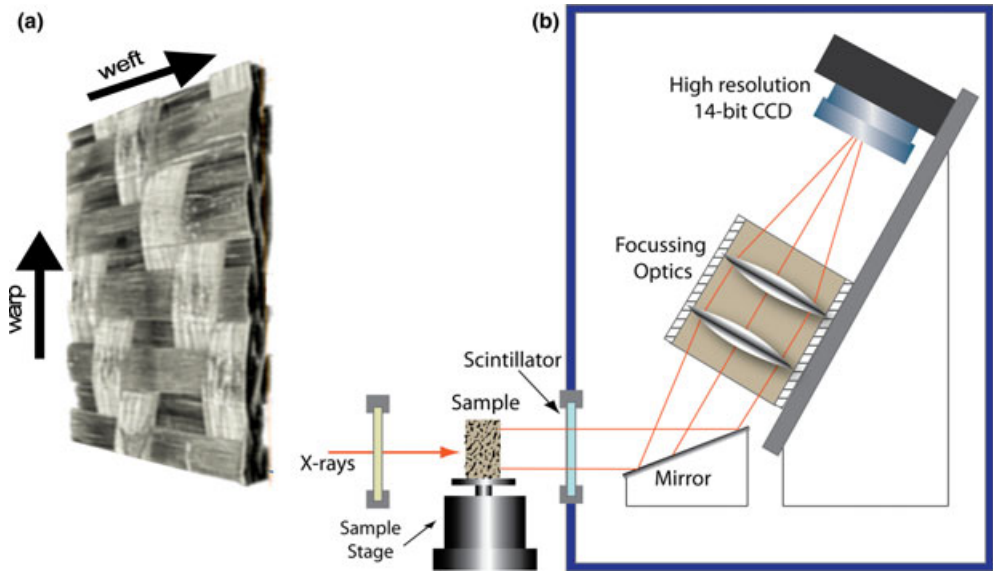

Fig. 1. (a) A 3-D image (acquired by methods described below) illustrates the 3-D woven character of the subject materials. (b) X-ray micro tomography setup at the 8.3.2 beamline at the advanced light source (ALS).

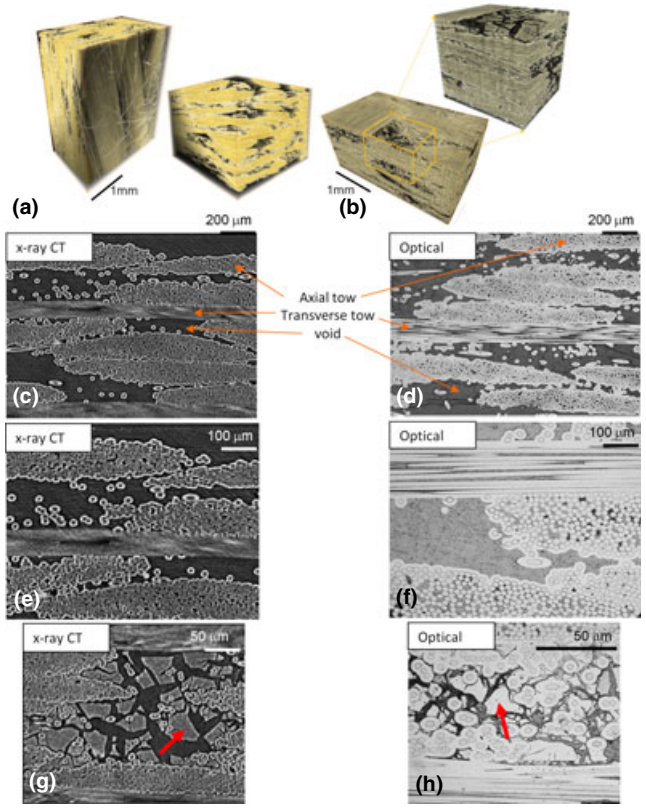

Fig. 2. (a) and (b) 3-D micro tomography images of SiC–SiC composite after the CVI processing step (a) and after the first polymer infiltration and pyrolysis step (b). (c) to (f) Comparison of optical images and micro tomography images (2-D reconstructed slices) from SiC–SiC composite after CVI processing. (g) and (h) Image comparison after first polymer infiltration and pyrolysis. (Arrows indicate SiC material formed by this infiltration cycle.)

structed 2-D axial slices (i.e., slices normal to the rotation axis) from both of these structures are compared with nominally equivalent optical images of polished cross sections prepared from other regions of the same composite in Figs. 2(c)–(h). This comparison serves to illustrate some of the capabilities and limitations of the tomographic images.

(i) The axial fiber tows are clearly outlined in the μCT images by the bright contrast of the layer of SiC that encases each tow.

(ii) The interior regions of the axial tows show mottled contrast that appears in places to correlate with individual fibers and gaps between fibers. However, the fibers and BN coatings are not resolved, as evidenced by the images of individual fibers that are separated from the tows: in the optical images, the SiC fiber, BN coating, and CVI SiC coating are clearly visible, whereas in the μCT image, these fibers appear as a bright ring surrounding a dark center. The intensity difference between this ring and the center is much greater than expected from possible differences in X-ray absorption between the outer CVI SiC coating and the inner BN-coated SiC fiber (which differ in density by less than 3%), suggesting a contribution from edge diffraction effects. Estimates of the lateral coherence length, which is related to the finite distance between the sample and source ($\sim$20 m), yield a few micrometer, comparable to the fiber diameter.

(iii) Blocks of SiC matrix material formed by pyrolysis of infiltrated polymer slurry are visible in Figs. 2(g)–(h). These blocks also show a bright outline in the μCT image, again suggesting edge diffraction effects, since in this case there is no change in material composition that could be responsible for the bright contrast around the edges.

(iv) The image detail is much better resolved within fibers and fiber tows oriented parallel to the rotation axis than in fiber tows oriented in the transverse direction possibly due to the large optical phase introduced by the fibers.[20]

(2) Carbon Fiber Textile Materials

The architecture of the three-layer angle interlock composite is shown in Fig. 3(a) in a section parallel to the warp fibers (the 3-D topology is defined completely below). A corresponding reconstructed axial tomography slice [Fig. 3(d)] can be compared with nominally equivalent optical images [Figs. 3(b) and (c)] of a polished cross section prepared from another region of the same composite. The optical images show the layer of CVI SiC encasing the tows, with limited

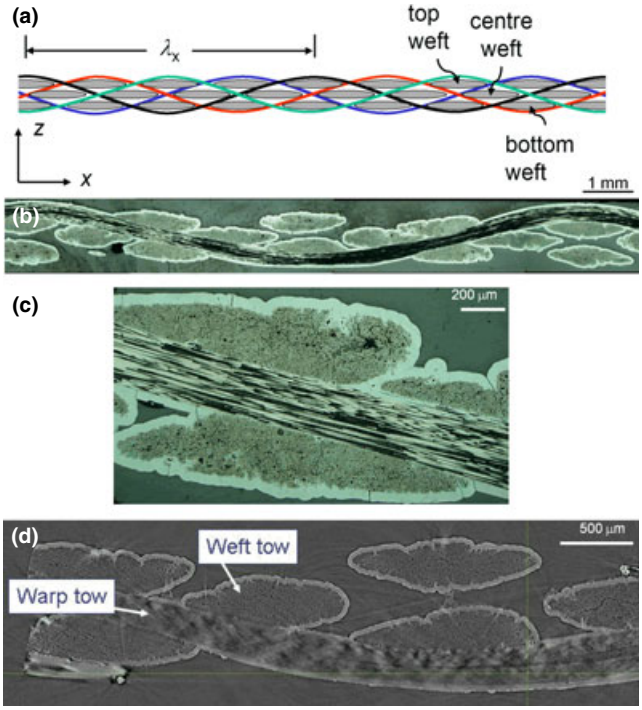

Fig. 3. (a) Schematic section of the subject three-layer angle interlock architecture along the warp direction (the (x, z) plane) showing projections of four warp tows as continuous curves and weft tows in section (ellipses). (b) and (c) Optical images of cross section from C-SiC composite corresponding to (a). (d) Micro tomography images corresponding to (a) (2-D reconstructed axial slice from C-SiC specimen with weft fiber tows parallel to rotation axis).

penetration of SiC between the carbon fibers in the interior of the tows. The SiC layer surrounding the tows is thicker (~40 μm) than in the SiC–SiC composite of Fig. 2 (~10 μm). It is also better resolved in the CT image of Fig. 3(d) than in Figs. 2(e) and (f). Other image characteristics in Fig. 3(d) are consistent with those described above for Fig. 2. There is a bright rim surrounding the SiC layer around the tows, although this is much less distinct than in Figs. 2(e) and (f); the image resolution is poor within the warp fiber tow, which was oriented normal to the rotation axis, while being relatively good in the weft fiber tows, which were oriented parallel to the axis.

IV. Acquisition of Tow Geometry

(1) Identification of the Spatial Domain Occupied by Each Tow

The 2-D image slices prepared as described above for the carbon fiber specimen were analyzed to identify the spatial domain occupied by each tow in the specimen. This process is called "image segmentation".[25] [‡‡] The spatial domain occupied by a tow is defined by the set of image pixels that are determined to lie within the tow; determining the domain therefore yields all the information available about the tow's geometry.

Image segmentation was carried out separately for the warp and weft tows, using 2-D image slices on which the tow being analyzed appeared in cross section. The segmentation sought to identify the boundaries of the section of the tow on the 2-D image. The complete 3-D tow domain could then be established by applying a 3-D region-growing algorithm to the entire image volume, stepping through the sequence of 2-D image slices.

The process of segmentation assigned a material identification label to each pixel by referring to intensity contrast, using a combination of an automated tool, the 3-D Visualization software Avizo v6.1 (VSG, Visualization Sciences Group, Inc., Burlington, MA) and manual steps to correct and complement the automated analysis. Contours were outlined along the tow boundaries using the edge detection lasso tool, by first drawing template contours manually with the assistance of the lasso tool after every 50 slices, and then generating successive contours using the slice interpolation tool within Avizo. This procedure involved manual generation of 62 contour slices in the axial direction and 40 slices in the transverse direction, with a total manual intervention time of ~6 h. Although more advanced algorithms exist for the automated segmentation,[26] their application would require higher resolution images than those available for the current study. The identification of tow boundaries was aided by the layer of SiC encasing the fiber tows, which had brighter pixel intensities than the interior of the tows.

The output file from the segmentation routine consists of individual warp and weft tow labels or reference codes assigned to tow spatial domains. The label file was converted into color codes to facilitate graphic presentation. Using the labels, the tows were converted to binary masks, i.e., binary labels attached to each pixel to tag whether it lies inside or outside a tow domain, which facilitated the statistical analysis of the tow geometry.

(2) Evaluation of Tow Parameters

Segmented axial and transverse mask data, i.e., spatial maps of tow domains, were imported as a stack into ImageJ, a JAVA based image processing tool (http://rsb.info.nih.gov/ij/). The reference codes of individual tows enable easy single tow selection. The mask data, having been defined using slices formed perpendicular to the tow axes, reveal cross-sectional features. Tow sections range in shape from blunt lenticular geometries to ellipses. The sectional shape of each tow on the 2-D slices, as revealed by the binary mask data, was fitted with an ellipse. More complex shapes could be chosen for fitting, to capture, for example, the flattened facets on the periphery of a tow where it contacts another tow. However, this is an unnecessary complication for the following reason: when the statistical data captured by the fitted ellipses are used to generate replicas of the imaged specimens (virtual specimens), flattened facets are introduced to remove interpenetrations, recreating the shape variations found in the real specimens. Thus, fitting ellipses to analyze images does not imply that other shape details are necessarily lost. The reader is referred to work to be published shortly for details.[27,28]

The operation of fitting ellipses yields the lengths of the major and minor axes of the fitted ellipse, the orientation of its axis system, its cross-sectional area, and the coordinates of its centroid. These data were recorded for every slice along the tow axis (at intervals equal to the pixel size of 4.4 μm). The process was carried out in both the axial and transverse directions throughout the 3-D specimen image, so that sections of both the warp and weft tows were fitted.

Reconstructed axial and transverse image slices from tiled scans of the C-SiC composite that was oriented with warp fiber tows aligned parallel to the rotation axis are shown in Fig. 4 (gray-scale images). Immediately above each gray-scale image is the corresponding map of segmented tows (tow domains distinguished by different colors). Superimposed on the gray-scale images are ellipses fitted to tow sections. A representation of the geometrical data for tows that are deduced from the fitted ellipses is shown merged with a 3-D rendering of the CT image in Fig. 5(c). The lines on the left side of the image [Fig. 5(c)] follow the loci of the tow cent-

[‡‡]Image segmentation is a step used in many applications in pattern recognition, computer vision, and image understanding to allow further image content exploitation in an efficient way. The process involves partitioning gray-level image into a number of regions, which are homogeneous according to some criteria and belong to either the foreground consisting of different material domains or the background.

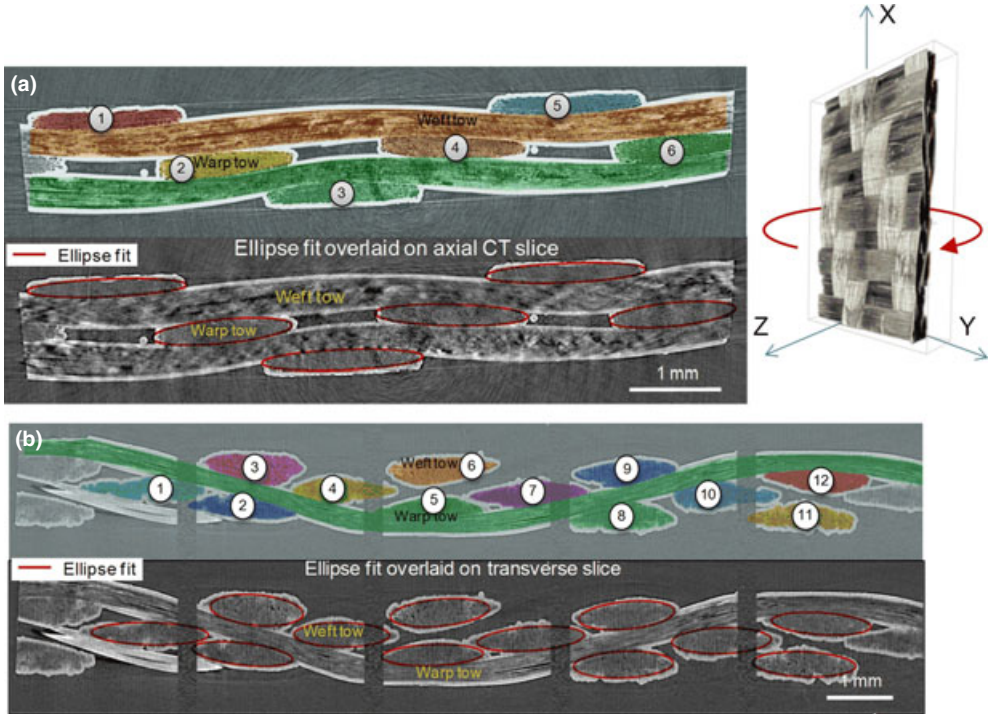

Fig. 4. Illustration of the segmented data set from three-layer angle-interlock C-SiC composite specimen oriented with warp fibers parallel to rotation axis. Colored and numbered regions in (a) and (b) indicate segmented regions (different tows). Fitted ellipses are marked on the gray-scale images.

roids, with the changing color along the lines representing the variations in tow cross-sectional area.

The angular orientations of individual tows perpendicular to the central axis of the tows and the cross-sectional areas are presented in Figs. 5(a) and (b). The overlaid picture of an actual sample on the tow plot indicates that variations in the orientation and areas of tows correlate with the locations of crossovers of weft and warp tows. Although small compared to the overall tow curvatures, the loci of the tow centroids possess noticeable deviations from their average waviness along the weft and warp directions.

V. Statistical Analysis of Tow Geometry

Discussion of statistical analysis will refer to the topological definition of the angle interlock architecture, which is defined by the cross-over patterns shown in Fig. 7. The CT image analysis yields quasi-continuous representations of tows, from which tow characteristics can be determined as functions of the position x or y (for warp or weft, Fig. 7) along the length of the tow. The tow characteristics analyzed consist of the locus of the centroid (or axis) of the tow, and the area, aspect ratio, and orientation of its cross section. The orientation of the cross section is defined so that a positive angle corresponds to clockwise rotation when viewed along the positive x-direction for warp tows or the positive y-direction for weft tows.

Qualitative inspection of the data for tow geometry suggests, as one would expect, that the geometrical characteristics possess periodic variations that correlate with the tow architecture (especially the locations of tow crossovers) together with stochastic deviations. A procedure was accordingly found that would deduce the periodic variations and stochastic deviations from the available image data and express them in simple parametric form. Prior works on the statistics of tow geometry did not partition variations into periodic systematic and non-periodic stochastic contributions, nor analyze the correlations of the latter along an individual tow or between tows.[16] The approach presented herein yields the input needed to generate virtual specimens that are statistically faithful to the measured composite samples, which can subsequently be used in predictions of performance.

Exploiting periodicity enables the maximum information to be deduced from relatively small CT specimens about both the non-stochastic, periodic (or "systematic") variations in tow geometry and deviations from the systematic behavior. However, the assumption that the textile fabric possesses periodicity in a spatially averaged sense is a strong one and needs independent testing; it requires the absence of distortions in the fabric over length scales much larger than the unit cell of the repeating structure. The required long-range uniformity in the rigidified carbon-fiber preform was confirmed by analyzing optical images of samples with linear dimensions many tens or a hundred times larger than a unit cell. Lines fitted to weave features confirm that the rigidified carbon-fiber weave is rectangular to within 1° over long distances and the tow spacing shows no long-range trend (Fig. 6).

The architecture of the three-layer angle interlock carbon-fiber preform is shown in Figs. 3 and 7. Data analysis begins with identifying genuses of nominally identical warp and weft tows. In this particular weave, all warp tows belong to a single genus. The unit cell of the weave contains four warp tows, each with period λ_x in the warp direction and separated by a nominal interval $\lambda_y/4$ in the weft direction (Fig. 7). Successive warp tows (tows with increasing y coordinate) are shifted by $-\lambda_x/4$ along the warp (positive x) direction.

In addition to the single warp tow genus, three genuses of weft tows can be distinguished, labeled top, center, and bottom (Fig. 3). Because of symmetry in the nominal weave architecture, the top and bottom weft tows might be supposed to belong to a single genus; however, data for the real composite show that the top and bottom weft tows are systematically displaced relative to one another in a manner that is inconsistent with the nominal weave description. The relative displacement is along the warp direction and is suspected to have arisen because the top weft tows are always beaten into the fabric before the bottom weft tows. Thus, the fabric is locally tighter due to the presence of the top weft tows when

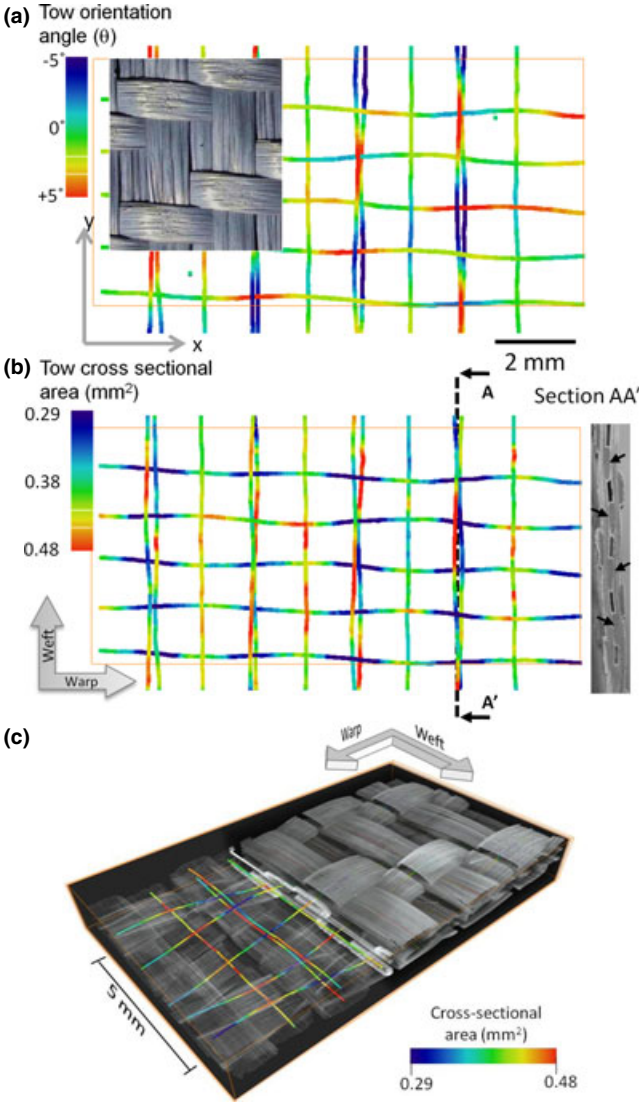

Fig. 5. Processed data from three-layer angle-interlock C-SiC composite showing top views of tow loci, with color representing (a) the tow orientation angles of warp and weft tows and (b) the cross-sectional area of weft and warp tows. The blue areas on the contours, for example, indicate smaller tow cross-sections resulting from compression between two weft tows. (c) 3-D reconstruction of tomography data from three-layer angle-interlock C-SiC composite, showing the warp and weft tows. The visualization includes tow loci (represented by colored lines) acquired through extraction of geometrical data from the tomograph. The loci represent the centroids, while variations in the cross-sectional area of the tows are shown in color.

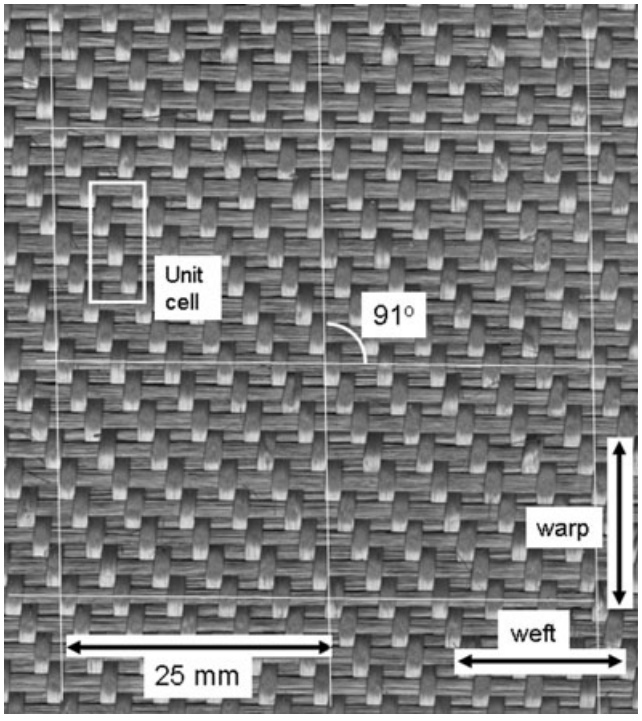

Fig. 6. Optical image of large samples of the subject carbon/SiC angle interlock weave confirms the absence of long-range distortions in the fabric.

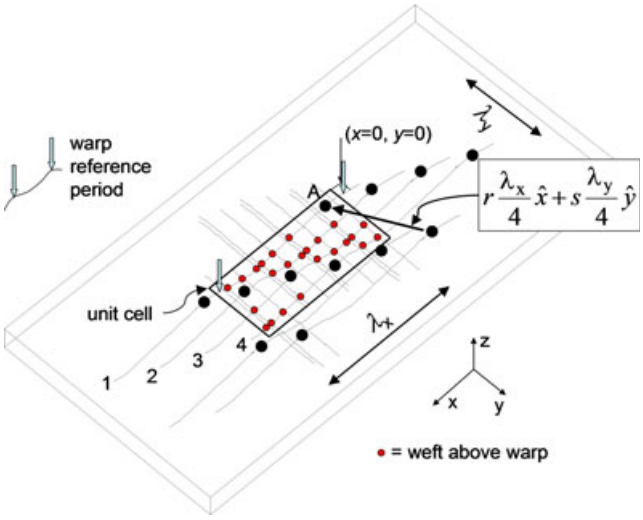

Fig. 7. 3-D plot of tow loci in the subject three-layer angle interlock architecture, showing the pattern of cross-overs within a single unit cell. One unit cell is marked in the (x, y) plane. The point marked A on warp tow 1 is equivalent, in the periodic average structure, to each of the other points on warp tows that are marked by large circles.

the bottom weft tows are beaten up, resulting in the bottom weft tows not pressing as far into the formed fabric as the top weft tows. This distinction of top and bottom weft tows in the sequence of loom actions breaks symmetry; the two types of tow are therefore assigned to distinct genuses.

All weft tows have a period λ_y in the weft direction. The weft tows in any genus are separated by $\lambda_x/4$ in the warp direction. In the coordinate system of Fig. 7, successive weft tows in any genus (tows with increasing y coordinate) are shifted by $-\lambda_y/4$ in the weft direction.

Absent stochastic deviations, any warp or weft tow can be made to coincide with any other tow of the same genus, and possess the same pattern of crossovers with orthogonal tows, by translating it through some vector $(r\lambda_x/4, s\lambda_y/4)$, with r and s integers. Thus, systematic variations of the four genuses of tows can be completely specified by determining the systematic variations of a single "reference" period for each genus of tow. The choice of reference period among the available data is arbitrary, because the structure is periodic; one possible choice for the warp tows in illustrated in Fig. 7.

(1) Determining Global Material Coordinates and the Unit Cell

Prior to statistical analysis, a global coordinate system (x, y, z) was determined that is aligned with the average tow orientations and corrects for any misalignment of the specimen relative to the weave during μCT data acquisition. This was done by analyzing the extrema in tow loci. It could have

been done alternatively using the systematic pattern of tow crossovers, but these correlate with the extrema and would therefore have given very similar results.

The x-axis, $\hat{x}$, or warp direction, was determined first as the average direction of all the vectors that could be formed between any two extrema residing on the same warp tow. The material z-axis, $\hat{z}$, was defined next as the vector orthogonal to $\hat{x}$ and a second vector that has the average direction of all the vectors that can be formed between any two extrema residing on different warp tows, with the restriction that the vectors have positive projections in the weft direction and join extrema that lie nominally in the same z-plane. The material y-axis, $\hat{y}$, is defined by the cross-product $\hat{y} = \hat{z} \times \hat{x}$.

With the above definition of material coordinates, the weft tows will not be aligned with the y-axis if the fabric possesses a global in-plane shear deformation. No such shear is evident for the weaves studied herein (Fig. 6).

With data transformed into the aligned system (x, y, z), the period λ_x is determined by calculating the average difference of the average x-coordinate of successive weft tows of the same genus ($=\lambda_x/4$) and the period λ_y is determined by calculating the average difference of the average y-coordinate of successive warp tows ($=\lambda_y/4$) (Table I).

(2) Defining a Grid for Data

In the statistical analysis, the characteristics of each tow are represented at a number of discrete material points, equally spaced along its axis. Data referring to this discrete grid are prepared for each tow genus using a procedure that is illustrated below for the tow centroid locus for warp tows. The procedures for weft tows and for tow cross-sectional areas, aspect ratios, and orientations are analogous.

First, an interval of length λ_x is chosen from the available data as the reference period (e.g., as marked by arrows in Fig. 7). A grid of N_φ equally spaced grid points is defined along this interval, the first lying at one end and the other a distance λ_x/N_φ short of the other. Thus, in the periodic structure of the systematic tow characteristics, point N_φ +1 will be equivalent to point 1. All data points on all warp tows can be associated with one of the N_φ grid points in the reference period by translating the point through some vector ($r\lambda_x/4$, $s\lambda_y/4$), with r and s integers (Fig. 7). A satisfactory choice is $N_\varphi = 24$, since this gives a grid spacing that is smaller than the period of systematic variations in all statistical quantities analyzed, and also smaller than the correlation lengths for their deviations. The same number of reference-period grid points are used for all tow genuses.

Suppose there are N_w warp tows in the CT data set. The data for the centroids of each warp tow consist of the set of coordinates $\{x^{(n,j,w)}, n = 1,.., n_j^{(w)}\}$, where $j = 1, \ldots, N_w$ is a label for that tow, $n_j^{(w)}$ is the number of data points along its length, and superscript w indicates the warp genus. The vector $\boldsymbol{x}^{(n,j,w)}$ contains the two coordinate components normal to the tow axis, e.g., the y and z coordinates of the tow centroids for warp tows. Let the compact notation (n, j) refer to the nth data point on tow j. All warp data points will be associated with one of the N_φ points in the reference period. Let $\Omega_\varphi^{(w)}$ denote the set of warp data points belonging to reference point $\varphi^{(w)}$ ($\varphi^{(w)} = 1,.., N_\varphi$).

(3) Determining Systematic Characteristics of Tow Loci

To identify systematic (average periodic) character in the CT data for tow centroids, the centroid coordinates (x, y, z) at any point (n, j) on a warp tow are decomposed into systematic and stochastic parts:

Table I. Dimensions of the Unit Cell (see Fig. 9)

Wavelength in the warp direction, λ_x	11.5 mm
Wavelength in the weft direction, λ_y	5.10 mm

$$(x,y,z)^{(n,j,w)} = \left\langle (x,y,z)^{(n,j,w)} \right\rangle + (\delta x, \delta y, \delta z)^{(n,j,w)} \tag{1a}$$

where $\langle .. \rangle$ denotes an average and

$$\left\langle (x,y,z)^{(n,j,w)} \right\rangle = u_\varphi^{(w)} + r\frac{\lambda_x}{4}\hat{x} + s\frac{\lambda_y}{4}\hat{y} \tag{1b}$$

with

$$u_\varphi^{(w)} = \frac{1}{m_\varphi}\sum_{\Omega_\varphi^{(w)}} \left((x,y,z)^{(n,j,w)} - r\frac{\lambda_x}{4}\hat{x} - s\frac{\lambda_y}{4}\hat{y} \right). \tag{1c}$$

The quantity $u_\varphi^{(w)}$ defines the systematic variation in the coordinates of the tow centroid; since the systematic variation is periodic, $u_\varphi^{(w)}$ only needs to be specified for each of the N_φ grid points of the reference period. The sum in Eq. (1c) is made over all the m_φ members of the set $\Omega_\varphi^{(w)}$. The integers r and s are those that translate each data point in Eqs. (1b) and (1c) to the reference point φ. Examples of this translation vector for one reference point are shown in Fig. 7.

The quantity $(\delta x, \delta y, \delta z)^{(n,j,w)}$ defines the deviation in the coordinates of the tow centroid, a random variable. Since x is an independent variable for warp tows, only δy and δz are nonzero for warp tows, and since y is an independent variable for weft tows, only δx and δz are nonzero for weft tows.

By the procedure of Eq. (1), the systematic coordinates of each point in the reference period are defined by using all the available data for that point that exist in the CT data set. Even for the small textile samples that can be examined at high resolution (~1 μm), the average refers typically to 5–10 data points; i.e., the sample contains 5–10 intervals on the different tows within it that are equivalent to the reference period chosen for any tow genus.

(4) Determining Stochastic Characteristics of Tow Loci

With $(x,y,z)^{(n,j,w)}$ determined, the stochastic part of the data point (n, j) is given by $(\delta x, \delta y, \delta z)^{(n,j,w)} = (x,y,z)^{(n,j,w)} - \left\langle (x,y,z)^{(n,j,w)} \right\rangle$. Several statistics of these deviations were examined.

The first is the root mean square deviation (RMSD) $\sigma^{(\delta y,w)}$ of $\delta y^{(n,j,w)}$ for a warp tow, which, since the mean of δy is zero, takes the form:

$$\sigma^{(\delta y,w)} = \sqrt{\sum \left(\delta y^{(n,j,w)}\right)^2 \Big/ n_{expt}} \tag{2a}$$

where the sum is performed over all n_{expt} available data points on warp tows. Similar expressions are obtained for $\sigma^{(\delta z,w)}$.

The second is Pearson's correlation parameter applied, e.g., to the values of δy for a warp tow (or, analogously, to δz) at pairs of data points separated by k grid points on the same tow:

$$C^{(\delta y,w)}(k) = \frac{\sum \delta y^{(n,j,w)} \delta y^{(n+k,j,w)} \big/ n n_{expt}}{\left(\sigma^{(\delta y,w)}\right)^2} \tag{2b}$$

where the sum is performed over all nn_{expt} available pairs of data points $\{(n, j), (n, j + k)\}$ on all warp tows. To ensure the bounds $-1 \leq C^{(\delta y,w)} \leq 1$, the denominator in Eq. (2b) must be formed by summing over the same set of data points that enter into the sum in the numerator. For deviations of the tow centroid that persist over wavelengths that are long relative to the separation of data points, $C^{(\delta y,w)}(1) \to 1$. As k increases, $C^{(\delta y,w)}$ generally decreases, indicating that the coordinate deviations on a tow become uncorrelated for well separated points. For small k, $C^{(\delta y,w)}(k) \approx 1 - kd/\zeta^{(\delta y,w)}$, where d is the distance between

successive grid points and $\zeta^{(\delta y,w)}$ is a correlation length for fluctuations of the x coordinate of the centroid of warp tows. (This is not to be confused with the wavelength of systematic coordinate variations; unlike the systematic variations, the coordinate deviations need not be periodic or exhibit correlation lengths that are commensurate with the textile architecture).

The RMSD and correlation parameter have been defined for warp tows. Similar statistics are defined for the three weft genuses using Eqs. (1) and (2) with the notation *tw*, *cw*, or *bw* replacing *w* for top weft, center weft, and bottom weft, respectively. Similar statistics are also defined for both warp and weft tows for the characteristics of the tow sections, with the notation A and δA, ar and δar, or θ and $\delta\theta$ replacing x and δx for the area, aspect ratio, or orientation of the section.

(5) Results for Systematic Variations of Tow Characteristics

The systematic variations of the coordinates of the centroids of warp tows show approximately sinusoidal variations (Fig. 8). However, sinusoidal fits to the data were not made and are unnecessary and undesirable; the systematic variations are deduced without imposing any parametric form. The motion of warp tows in the z-direction exhibits a single cycle per period of the textile architecture, as might be expected (Fig. 3). But interestingly, their motion in the y-direction exhibits two cycles in the same distance.

The systematic variations of the area and aspect ratio of sections of the warp tows show four cycles per period, equal to the total number of crossovers with weft tows of all type [Figs. 9(a) and (b)]. Of note is that:

1. The orientation of warp tow sections varies relatively irregularly [Fig. 9(c)].
2. The systematic variations of the coordinates of the centroids of weft tows show qualitatively similar periodic variations to those of warp tows, except that the z-coordinate lacks the large amplitude oscillations of the warp tows.
3. The systematic variations of the sectional parameters of weft tows mostly lack the multiple cyclic variations seen in Figs. 9(a) and (b).

Mean values of the tow section areas differ by only a few percent for different tow genuses, whereas the aspect ratio varies by ±20% (Table II). The mean orientation for all ge-

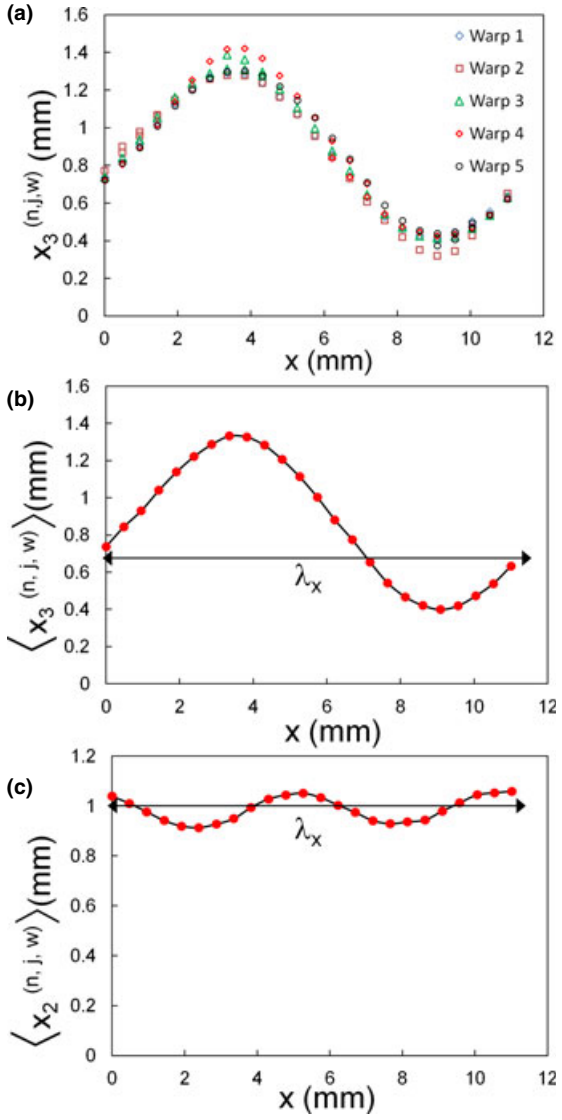

Fig. 8. The coordinates of the centroid of warp tows. (a) Data for the z-coordinate from all warp tows collated onto a single reference period by translation operations. (b) Systematic variations of the z-coordinate formed by averaging the data in (a). (c) Systematic variations of the y-coordinate.

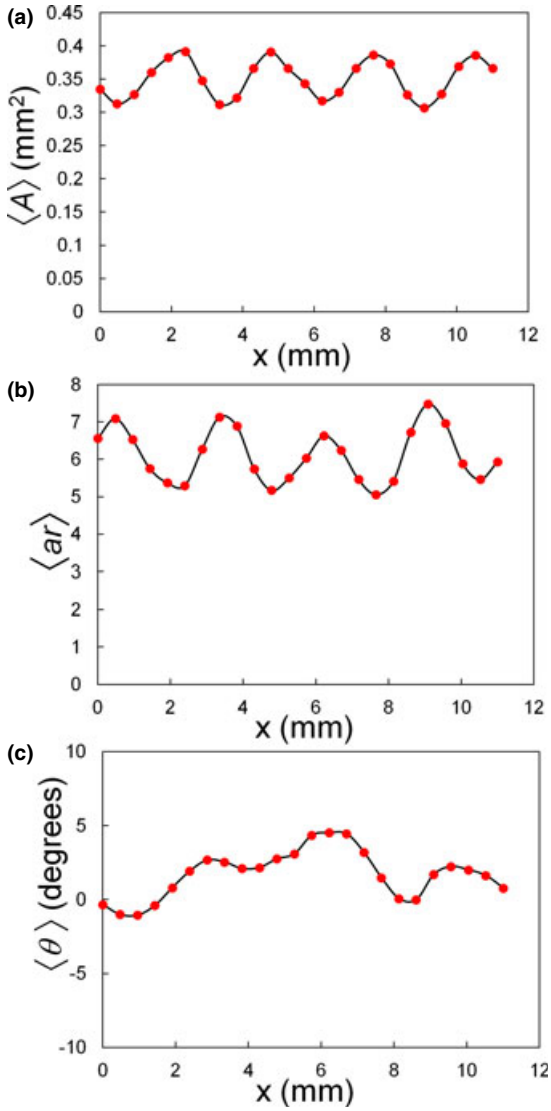

Fig. 9. Systematic variations in the sections of warp tows along the same reference period that was used in Fig. 9. (a) Cross-sectional area; (b) aspect ratio; (c) orientation.

nuses is close to 0°, but the systematic variations in section orientation range up to ±5° (Table II, Fig. 9(c), and other data).

(6) Results for Stochastic Variations of Tow Characteristics

The complete set of statistical measures for individual tow genuses appears in Table III. The largest absolute deviations from the systematic variations in tow centroid coordinates are those of weft tows in the x-direction (lateral displacements in the warp direction). All absolute deviations are small compared to the width dimensions of the tows (~0.24 mm in the z-direction and 1.25 mm in the in-plane direction), indicating that good control was maintained in the weaving process. Nevertheless, deviations will commonly occur in larger components (e.g., 0.1 m in dimension) that are of order of magnitude 2× RMSD, or ~10% of either tow width. Such deviations may perturb the local tow density and orientations sufficiently to affect local failure events, a topic to be addressed elsewhere.

Deviations in the area of tow sections range up to 5% and those in the aspect ratio up to 10%. Deviations in the orientation of sections are less than 1°, or 20% of the amplitude of systematic orientation variations.

The correlation lengths for deviations in tow centroid coordinates or tow section areas are similar to the spacing of crossovers (2–4 mm). The correlation lengths for deviations in the tow aspect ratio or orientation are much larger (mostly 6–16 mm), comparable to the unit cell dimensions.

The deviations in the coordinates of the tow centroids are normally distributed over most of the range of the variable (linear plot in Fig. 10). Departures from linearity at the extremes for δz suggest that the distribution is a truncated normal distribution, with maximum deviation ≈2 standard deviations (the weave evidently suppresses very large through-thickness deviations).

Distribution tests similar to those in Fig. 10 were also applied to the area, aspect ratio, and orientation of the tow sections. Similar qualitative observations apply; normal distributions prevail, except that, like δz, distributions of the area and aspect ratio of the central weft tows appear to be truncated at ≈2 standard deviations (Fig. 11).

(7) Correlations Between Different Tows at Crossovers

Further statistics that were examined refer to the correlations between components of the deviation vectors, $(\delta x, \delta y, \delta z)^{(\mathrm{n,j,w})}$, $(\delta x, \delta y, \delta z)^{(\mathrm{n,j,tw})}$, $(\delta x, \delta y, \delta z)^{(\mathrm{n,j,cw})}$, and $(\delta x, \delta y, \delta z)^{(\mathrm{n,j,bw})}$ associated with different tow genuses. Key statistics are the inter-tow correlations at cross-over points, where one warp and one weft tow contact each other. The cross-over points are defined as the intersections of the loci of the centroids of the two tows when projected on the (x, y) plane. The correlations between different components of the deviation vector for the tow centroids at crossovers are negligible, except between the component in the z-direction for different tows (Table IV).

VI. Summary and Conclusions

Three-dimensional images from high-intensity X-ray micro computed tomography have been demonstrated with resolution of some features that are comparable to the fiber diameter. This is sufficient to monitor key microstructural developments occurring during cycles of matrix infiltration into a multi-ply SiC–SiC composite. However, low contrast between SiC fibers and a SiC matrix prevent individual fibers within tows from being resolved individually at the resolution used to scan the entire samples. Contrast between entire tows can be achieved more easily, because of the CVI coating applied to tows in the materials studied. Thus, the complete 3-D spatial coordinates of individual tows in a three-layer angle interlock textile composite could be determined.

For textile composites, the substantial scatter commonly observed in strength and fatigue life is closely linked to geometrical defects or irregularities in the reinforcement geometry. The rich 3-D data exemplified by the data in this article therefore constitute a major necessary first step toward linking strength and fatigue life to the microstructure of textile composites.

Table II. Averages of Tow Cross-Sectional Parameters

	Area, A (mm^2)	Aspect ratio, ar	Orientation, θ (degrees)
Warp	0.35	6.3	2.0
Top weft	0.38	4.6	0.0
Center weft	0.40	5.4	1.5
Bottom weft	0.38	5.2	-1.0

Table III. RMSD and Correlation Length for the Stochastic Tow Parameters

(a) Warp tows

$\sigma^{(\delta y,\mathrm{w})}$ (mm)	$\zeta^{(\delta y,\mathrm{w})}$ (mm)	$\sigma^{(\delta z,\mathrm{w})}$ (mm)	$\zeta^{(\delta z,\mathrm{w})}$ (mm)	$\sigma^{(A,w)}$ (mm^2)	$\zeta^{(A,\mathrm{w})}$ (mm)	$\sigma^{(\mathrm{ar,w})}$	$\zeta^{(\mathrm{ar,w})}$ (mm)	$\sigma^{(\theta,\mathrm{w})}$ (deg.)	$\zeta^{(\theta,\mathrm{w})}$ (mm)
0.021	3.5	0.034	3.65	0.017	3.4	0.787	10.6	0.890	4.2

(b) Top weft tows

$\sigma^{(\delta x,\mathrm{tw})}$ (mm)	$\zeta^{(\delta x,\mathrm{tw})}$ (mm)	$\sigma^{(\delta z,\mathrm{tw})}$ (mm)	$\zeta^{(\delta z,\mathrm{tw})}$ (mm)	$\sigma^{(A,\mathrm{tw})}$ (mm^2)	$\zeta^{(A,\mathrm{tw})}$ (mm)	$\sigma^{(\mathrm{ar,tw})}$	$\zeta^{(\mathrm{ar,tw})}$ (mm)	$\sigma^{(\theta,\mathrm{tw})}$ (deg.)	$\zeta^{(\theta,\mathrm{tw})}$ (mm)
0.068	3.4	0.029	5.3	0.010	3.1	0.302	20.3	0.775	7.9

(c) Center weft tows

$\sigma^{(\delta x,\mathrm{cw})}$ (mm)	$\zeta^{(\delta x,\mathrm{cw})}$ (mm)	$\sigma^{(\delta z,\mathrm{cw})}$ (mm)	$\zeta^{(\delta z,\mathrm{cw})}$ (mm)	$\sigma^{(A,\mathrm{cw})}$ (mm^2)	$\zeta^{(A,\mathrm{cw})}$ (mm)	$\sigma^{(\mathrm{ar,cw})}$	$\zeta^{(\mathrm{ar,cw})}$ (mm)	$\sigma^{(\theta,\mathrm{cw})}$ (deg.)	$\zeta^{(\theta,\mathrm{cw})}$ (mm)
0.077	3.9	0.016	5.9	0.015	3.4	0.706	16.7	0.925	16.6

(d) Bottom weft tows

$\sigma^{(\delta x,\mathrm{bw})}$ (mm)	$\zeta^{(\delta x,\mathrm{bw})}$ (mm)	$\sigma^{(\delta z,\mathrm{bw})}$ (mm)	$\zeta^{(\delta z,\mathrm{bw})}$ (mm)	$\sigma^{(A,\mathrm{bw})}$ (mm^2)	$\zeta^{(A,\mathrm{bw})}$ (mm)	$\sigma^{(\mathrm{ar,bw})}$	$\zeta^{(\mathrm{ar,bw})}$ (mm)	$\sigma^{(\theta,\mathrm{bw})}$ (deg.)	$\zeta^{(\theta,\mathrm{bw})}$ (mm)
0.071	4.0	0.024	4.5	0.015	3.8	0.337	6.3	0.939	13.1

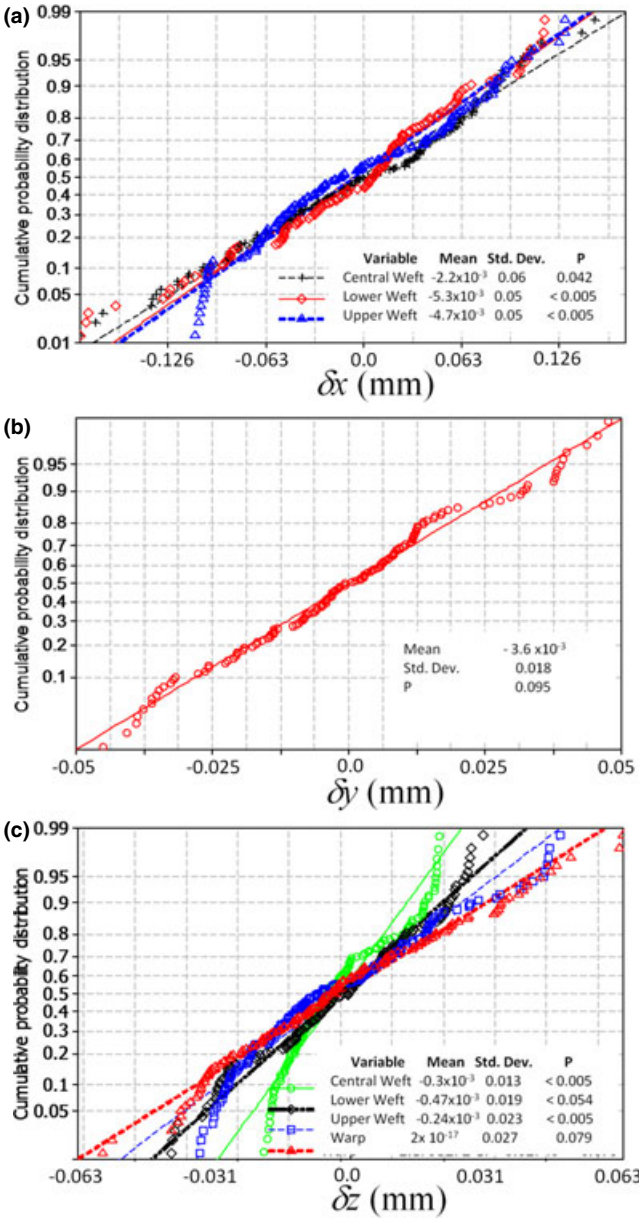

Fig. 10. Cumulative probability distributions of the deviations in the coordinates of the tow centroids from their non-stochastic, periodic variations. The ordinate is scaled by the error function, so that normally distributed data fall on straight lines. Data for the carbon fiber angle interlock weave.

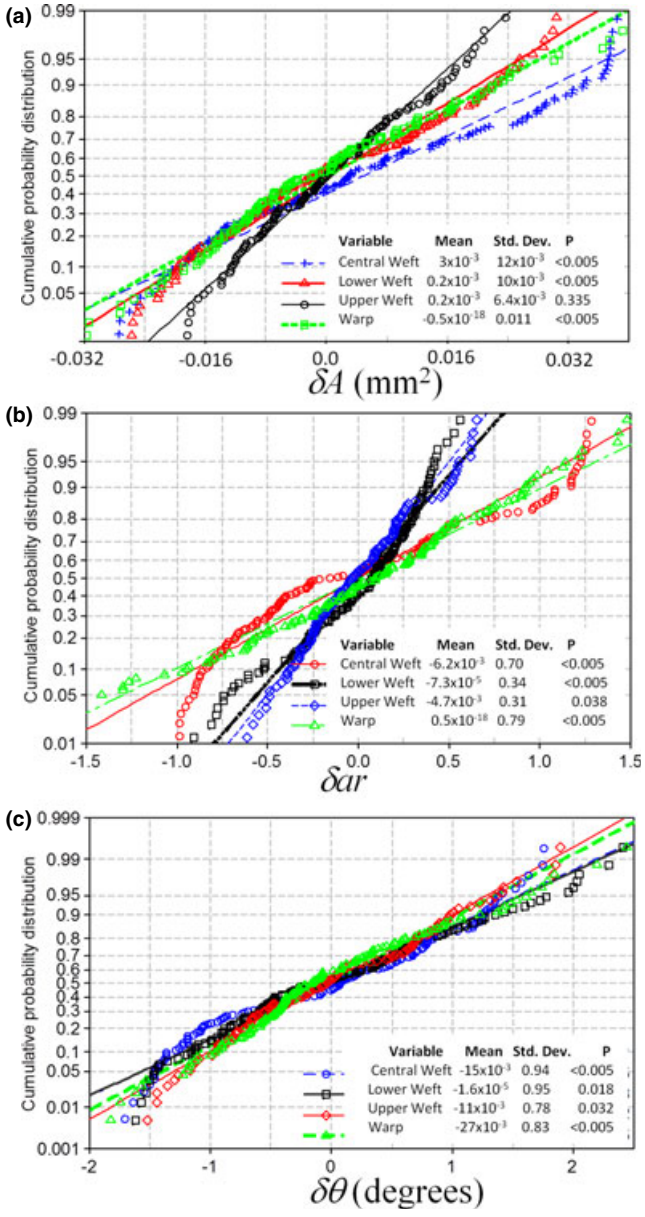

Fig. 11. Cumulative probability distributions of the deviations in (a) the tow cross-sectional area, (b) the tow orientation angle, and (c) the tow aspect ratio. Other details as in Fig. 10.

The data have proven amenable to representation by a relatively limited set of characteristics, namely the tow centroids and the area, aspect ratio, and orientation of the tow cross sections. All this information can be summarized by simple numerical records of non-stochastic, periodic variations in tows, together with a handful of scalar statistical parameters that characterize non-periodic, stochastic deviations. Exploiting the nominal periodicity of the textile reinforcement maximizes the information that can be deduced from relatively small μCT specimens and provides a route to generating virtual specimens that are much larger than the imaged specimens, which will be pursued in forthcoming articles.

Key features in the measured non-stochastic periodic geometrical characteristics include variations of tow positioning both up and down and side to side; substantial variations in the area and aspect ratio of sections and rotations of tows along their length, and the presence of cyclic variations of characteristics over wavelengths different from the period of the textile unit cell. Correlation lengths for tow positioning, and for variations in the area, aspect ratio, and orientation of cross sections, show significant differences in magnitude. Correlations for the centroid position between different tows at tow crossovers are small with the exception of deviations in the through-thickness direction. The set of correlations has important implications for formulating a probabilistic model to generate statistically faithful replicas of the specimens studied herein, which will be taken up elsewhere.

Table IV. Correlations Between Components of Deviation Vectors at Cross-Overs

	$\delta x^{(tw)}$	$\delta z^{(tw)}$	$\delta x^{(cw)}$	$\delta z^{(cw)}$	$\delta x^{(bw)}$	$\delta z^{(bw)}$
$\delta y^{(w)}$	−0.048	−0.418	−0.203	−0.228	0.312	0.057
$\delta z^{(w)}$	0.213	0.910	0.481	0.793	−0.055	0.877

Acknowledgment

We thank Dr. Alastair MacDowell at the ALS for help with the tomography.

References

[1]B. N. Cox, M. S. Dadkhah, R. V. Inman, W. L. Morris, and J. Zupon, "Mechanisms of Compressive Failure in 3D Composites," *Acta Metall. Mater*., **40**, 3285–98 (1992).

[2]B. N. Cox, M. S. Dadkhah, and W. L. Morris, "On the Tensile Failure of 3D Woven Composites," *Composites*, **27A**, 447–58 (1996).

[3]B. N. Cox, M. S. Dadkhah, W. L. Morris, and J. G. Flintoff, "Failure Mechanisms of 3D Woven Composites in Tension, Compression, and Bending," *Acta Metall. Mater*., **42**, 3967–84 (1994).

[4]M. S. Dadkhah, J. G. Flintoff, T. Kniveton, and B. N. Cox, "Simple Models for Triaxially Braided Composites," *Composites*, **26**, 91–102 (1995).

[5]M. S. Dadkhah, W. L. Morris, and B. N. Cox, "Compression-Compression Fatigue in 3D Woven Composites," *Acta Metall. Mater*., **43** [12] 4235–45 (1995).

[6]S. P. Lomov and I. Verpoest, "Compression of Woven Reinforcements: A Mathematical Model," *J. Reinf. Plast. Compos*., **19**, 1329–50 (2000).

[7]A. C. Long, B. J. Souter, F. Robitaille, and C. D. Rudd, "Effects of Fibre Architecture on Reinforcement Fabric Deformation," *Plast. Rubber Compos*., **31** [2] 87–97 (2002).

[8]Y. Miao, E. Zhou, Y. Q. Wang, and B. A. Cheeseman, "Mechanics of Textile Mechanics: Micro-Geometry," *Compos. Sci. Technol*., **68** [7–8] 1671–8 (2008).

[9]D. B. Marshall and B. N. Cox, "Integral Textile Ceramic Structures," *Ann. Rev. Mater. Res*., **38**, 425–43 (2008).

[10]A. J. Moffat, P. Wright, J. Y. Buffiere, I. Sinclair, and S. M. Spearing, "Micromechanisms of Damage in 0 Degrees Splits in a 90/0 (s) Composite Material Using Synchrotron Radiation Computed Tomography," *Scr. Mater*., **59** [10] 1043–6 (2008).

[11]G. N. Morscher, H. M. Yun, and J. A. DiCarlo, "In-Plane Cracking Behavior and Ultimate Strength for 2D Woven and Braided Melt-Infiltrated SiC/SiC Composites Tensile Loaded in Off-Axis Fiber Directions," *J. Am. Ceram. Soc*., **90** [10] 3185–93 (2007).

[12]H. M. Yun and J. A. DiCarlo, "Through-Thickness Properties of 2D Woven SiC/SiC Panels with Various Microstructures," *Ceram. Eng. Sci. Proc*., **25** [4] 71–8 (2004).

[13]H. M. Yun, J. Z. Gyekenyesi, and J. A. DiCarlo, "Effects of 3D-Fiber Architecture on Tensile Stress-Strain Behavior of SiC/SiC Composites," *Ceram. Eng. Sci. Proc*., **23** [3] 503–10 (2002).

[14]G. N. Morscher, J. A. DiCarlo, J. D. Kiser, and H. M. Yun, "Effects of Fiber Architecture on Matrix Cracking for Melt-Infiltrated SiC/SiC Composites," *Int. J. Appl. Ceram. Technol*., **7** [3] 276–90 (2010).

[15]P. Badel, E. Vidal-Salle, E. Maire, and P. Boisse, "Simulation and Tomography Analysis of Textile Composite Reinforcement Deformation at the Mesoscopic Scale," *Compos. Sci. Technol*., **68**, 2433–40 (2008).

[16]F. Desplentere, S. V. Lomov, D. L. Woerdeman, I. Verpoest, M. Wevers, and A. E. Bogdanovich, "Micro-CT Characterization of Variability in 3D Textile Architecture," *Compos. Sci. Technol*., **65**, 1920–30 (2005).

[17]Y. Mahadik, K. A. Robson Brown, and S. R. Hallett, "Characterisation of 3D Woven Composite Internal Architecture and Effect of Compaction," *Compos. Part A*, **41**, 872–80 (2010).

[18]S.-B. Lee, S. R. Stock, M. D. Butts, T. L. Starr, T. M. Breunig, and J. H. Kinney, "Pore Geometry in Woven Fiber Structures: 0/90 Plain-Weave Cloth Layup Preform," *J. Mater. Res*., **13** [5] 1209–17 (1998).

[19]J. H. Kinney, T. M. Breunig, T. L. Starr, D. Haupt, M. C. Nichols, S. R. Stock, M. D. Butts, and R. A. Saroyan, "X-ray Tomographic Study of Chemical Vapor Infiltration Processing of Ceramic Composites," *Science*, **260**, 789–92 (1993).

[20]O. Coindreau, G. Vignoles, and P. Cloetens, "Direct 3D Microscale Imaging of Carbon-Carbon Composites with Computed Holotomography," *Nucl. Instrum. Methods Phys. Res. B*, **200**, 308–14 (2003).

[21]P. Wright, X. Fu, I. Sinclair, and S. M. Spearing, "Ultra High Resolution Computed Tomography of Damage in Notched Carbon Fiber-Epoxy Composites," *J. Compos. Mater*., **42** [19] 1993–2002 (2008).

[22]W. B. Hillig, "Effect of Fibre Misalignment on the Fracture Behaviour of Fibre-Reinforced Composites. Part I. Experimental," *J. Mater. Sci*., **29**, 419–23 (1994).

[23]S. W. Yurgatis, "Measurement of Small Angle Fiber Misalignments in Continuous Fiber Composites," *Compos. Sci. Technol*., **30**, 279–93 (1987).

[24]C. E. Duchon, "Lanczos Filtering in One and Two Dimensions," *J. Appl. Meteorol*., **18** [8] 1016–22 (1979).

[25]M. Frucci and G. Sanniti di Baja, "From Segmentation to Binarization of Gray-Level Images," *J. Pattern Recogn. Res*., **20**, 1–13 (2008).

[26]J. Martın-Herrero and C. Germain, "Microstructure Reconstruction of Fibrous C-C Composites from XMCT," *Carbon*, **45**, 1242–53 (2007).

[27]M. Blacklock, H. Bale, M. R. Begley, and B. N. Cox, "Generating virtual textile composite specimens using statistical data from micro-computed tomography: I. 1D tow representations for the Binary Model," *J. Mech. Phys. Solids*, in review (2011).

[28]R. Rinaldi, M. Blacklock, H. Bale, M. R. Begley, and B. N. Cox, "Generating virtual textile composite specimens using statistical data from micro-computed tomography: II. 3D tow representations," *J. Mech. Phys. Solids*, in review (2011). □